

The nature of the jet-driven outflow in the radio galaxy 3C 305

M.J. Hardcastle^{1*}, F. Massaro^{2,3}, D.E. Harris², S.A. Baum^{4,5}, S. Bianchi⁶,
M. Chiaberge^{7,8,9}, R. Morganti^{10,11}, C.P. O’Dea^{12,2}, and A. Siemiginowska²

¹ School of Physics, Astronomy & Mathematics, University of Hertfordshire, College Lane, Hatfield AL10 9AB, UK

² Harvard-Smithsonian Center for Astrophysics, 60 Garden Street, Cambridge, MA 02138, USA

³ SLAC National Laboratory and Kavli Institute for Particle Astrophysics and Cosmology, 2575 Sand Hill Road, Menlo Park, CA 94025, USA

⁴ Chester F. Carlson Center for Imaging Science, Rochester Institute of Technology, Rochester, NY 14623, USA

⁵ Radcliffe Institute for Advanced Study, 10 Garden Street, Cambridge, MA 02138, USA

⁶ Dipartimento di Fisica, Università degli Studi Roma Tre, via della Vasca Navale 84, 00146 Roma, Italy

⁷ Space Telescope Science Institute, Baltimore, MD 21218, USA

⁸ Center for Astrophysical Sciences, Johns Hopkins University, 3400 N. Charles Street Baltimore, MD 21218, USA

⁹ INAF - Istituto di Radioastronomia di Bologna, via Gobetti 101 40129 Bologna, Italy

¹⁰ ASTRON, P.O. Box 2, 7990 AA Dwingeloo, The Netherlands

¹¹ Kapteyn Astronomical Institute, University of Groningen, P.O. Box 800, 9700 AV Groningen, The Netherlands

¹² Department of Physics, Rochester Institute of Technology, 54 Lomb Memorial Drive, Rochester, NY 14623, USA

27 January 2021

ABSTRACT

We present *Chandra* X-ray and VLA radio observations of the radio galaxy 3C 305. The X-ray observations reveal the details of the previously known extended X-ray halo around the radio galaxy. We show using X-ray spectroscopy that the X-ray emission is consistent with being shock-heated material and can be modelled with standard collisional-ionization models, rather than being photoionized by the active nucleus. On this basis, we can make a self-consistent model in which the X-ray-emitting plasma is responsible for the depolarization of some regions of the radio emission from the jets and hotspots, and to place lower and upper limits on the magnetic field strength in the depolarizing medium. On the assumption that the X-ray-emitting material, together with the previously-known extended emission-line region and the outflow in neutral hydrogen, are all being driven out of the centre of the galaxy by an interaction with the jets, we derive a detailed energy budget for the radio galaxy, showing that the X-ray-emitting gas dominates the other phases in terms of its energy content. The power supplied by the jets must be $\sim 10^{43}$ erg s⁻¹.

Key words: galaxies: jets – galaxies: individual (3C 305) – galaxies: ISM – X-rays: galaxies

1 INTRODUCTION

In powerful radio galaxies, extended optical emission-line regions (EELR) are often found to be aligned with the axis defined by the extended radio emission (e.g., McCarthy et al. 1987; McCarthy 1993; McCarthy et al. 1996). A long-standing question (e.g., Baum & Heckman 1989; Tadhunter et al. 1998) is whether these EELR are ionized by photons from the nucleus or by shocks driven by the jets; in the most powerful radio sources, normally found at high redshift, there is often evidence that the optical emission-line material is either ionized or at least strongly affected by jet-driven shocks, which requires a direct interaction between the jets and the warm/cold ($T < 10^4$ K) phase of the ISM of the host galaxy (e.g., Sólórzano-Iñarrea et al. 2002; Nesvadba et al. 2008).

Where there is evidence for interaction between the jets and

the optical emission-line properties, the optical lines can be used to probe the *dynamics* of the material interacting with the radio source, since accurate radial velocities can be measured. It then becomes clear in many cases that the radio source drives a large-scale outflow, at least in the warm-gas phase, with typical speeds of hundreds of km s⁻¹ (e.g., O’Dea et al. 2002). The mass of the emission-line material itself is small, but its filling factor is necessarily very low, so that it is probably being driven out together with a much larger mass of material at some other temperature or ionization state. At least two components of this additional material must be present. On the one hand, it has recently been shown (e.g., Morganti, Tadhunter & Oosterloo 2005b) that at low redshift these sources often drive large-scale outflows of neutral hydrogen (i.e., colder gas) with very similar velocities. On the other, observations of radio depolarization associated with the extended emission-line regions (Heckman et al. 1982, 1984; Hardcastle et al. 1997) require the presence of a massive, ionized (i.e., warm-hot), magnetized

* E-mail: m.j.hardcastle@herts.ac.uk

medium in which the emission-line clouds are embedded (Hardcastle 2003). The precise mechanism of the interaction between the radio jets and these other phases of the ISM is not clear, but it makes radio-galaxy driven extended emission-line regions into objects of great interest for models of galaxy formation and evolution, since they provide a *kinetically*, rather than radiatively, driven method by which the central AGN can expel cold/warm gas from the center of the host galaxy (e.g., Tadhunter 2007).

The most recent clues to the nature of these interactions have come from X-ray observations with *Chandra*. In Hardcastle et al. (2010; hereafter H10) we presented observations of the intermediate-redshift, powerful radio galaxy 3C 171 ($z = 0.2384$), which has long been known to be associated with an emission-line outflow and with strong radio depolarization (e.g., Clark et al. 1998; Hardcastle et al. 2003). The *Chandra* observations revealed an extended X-ray region that was close to co-spatial with the emission-line material as seen in [OIII], [OII] and $H\alpha$, and also very well aligned with the region of radio depolarization. Morphologically this allowed us to rule out non-thermal (e.g., X-ray synchrotron) models for the X-rays. In interpreting the physics of X-rays associated with emission-line regions it is important to try to distinguish between photoionized and collisionally ionized X-ray-emitting material, since it is known (e.g., Bianchi et al. 2006) that in local Seyfert galaxies photoionization dominates. This was impossible in 3C 171 from direct observations of the X-ray spectrum (although photoionization was disfavored by morphological and energetic arguments) but we were able to estimate a temperature and density in the extended structures on the assumption of a collisional-ionization model, and then to show that this was consistent with the properties of the line-emitting gas and with the constraints from radio depolarization. A photoionization model would not be consistent with these observations. We were therefore able to estimate the mass of the X-ray-emitting material and to show that, on the assumption that this material is shocked gas flowing out along with the emission-line clouds, it completely dominates the energetics of the outflow; the total power in the outflow over the source lifetime was $\sim 3 \times 10^{44}$ erg s^{-1} , comparable to the bolometric radiative power of the AGN. We argued that 3C 171 is an analogue, presumably driven by a recent gas-rich merger, of the somewhat more powerful and much more common systems with extended X-ray emission and optical emission lines at high redshift (e.g., PKS 1138–262 at $z = 2.2$, Carilli et al. 2002) but with the advantage of being at low redshift and thus capable of being studied at high spatial resolution.

In this paper we discuss similarly motivated *Chandra* and radio observations of the nearby radio galaxy 3C 305. 3C 305 is a low-redshift radio galaxy which has been extensively studied because of its peculiar radio structure (Heckman et al. 1982, hereafter H82): its bright jets and hotspots are embedded in a pair of lobes which are much longer perpendicular to the jet axis than the core-hotspot distance. Its 178-MHz radio luminosity is 5.5×10^{24} W $Hz^{-1} sr^{-1}$, which puts it right on the FRI/FRII luminosity boundary of Fanaroff & Riley (1974). On the strict morphological definition, its distorted radio structure (Heckman et al. 1982) makes it an FRI (that is, the brightness in a low-resolution map would be peaked closer to the centre than the edges of the structure) and it is classed as such in catalogues such as that of Laing, Riley & Longair (1983). However, high-resolution radio imaging (e.g. Jackson et al. 2003, and this paper) clearly shows it to have jets and hotspots that are more characteristic of FRIIs.

3C 305 is similar to 3C 171 in many ways: it is a powerful radio galaxy of unusual morphology that is well known to be as-

sociated with an extended emission-line region on scales of the jets/hotspots, and to have strong co-spatial radio depolarization (H82); there is strong evidence in the case of 3C 305, e.g., from its morphology and from the detection of [FeII] emission peaked around the jet termination point, that the optical emission-line region is collisionally ionized (e.g., Jackson et al. 2003); and, crucially, it has a known association between the emission-line gas and X-ray emission on scales that are well resolved by *Chandra* (Massaro et al. 2009, hereafter M09; Fig. 1), discovered, like 3C 171's, as a result of the 'snapshot survey' of 3CR radio galaxies (Massaro et al. 2010). However, it differs in four key respects: 1) it is significantly lower in redshift ($z = 0.0416$), and physically smaller, so better matched to the scales of the host galaxy ISM; 2) its bright, relatively isolated host galaxy, IC 1065, is relatively well-studied and is known to show strong morphological and dynamical peculiarities consistent with being a recent merger involving at least one gas-rich spiral (Heckman et al. 1985); 3) it exhibits one of the best-studied examples of an association between the radio jets and an HI outflow (Morganti et al. 2005a); and 4) it is significantly (a factor ~ 4) brighter in extended X-rays than 3C 171. 3C 305 could be considered as a prototypical example of a young, galaxy-scale powerful radio source driven by galaxy-galaxy interactions, as expected in models of galaxy formation in the early universe, and, as emphasised by Morganti et al. (2005b), the presence of both warm and cold phases of the gas in the fast outflow already represents a challenge for models describing the interaction between radio jets and their environment.

In the present paper we present new *Chandra* and radio observations (Section 2) which give us the most sensitive X-ray image, and the most sensitive and highest-resolution radio images yet made of 3C 305. We show that the depolarized regions of radio emission become polarized again at high frequency, allowing the techniques developed by H10 to be applied to this source (Section 3). The new *Chandra* images confirm that the extended X-ray emission is morphologically very similar to the previously known emission-line nebula, but also show some important differences (Section 4); there is no evidence for large-scale X-ray emission from a group or cluster environment, and the X-ray spectrum of the extended emission is consistent with being thermal emission from the ISM of the host galaxy shocked by the jets. In Section 5 we combine the available data to show that it is plausible that the X-ray-emitting gas is the depolarizing medium, and use the picture of the source implied by these measurements to estimate its energy budget. Our conclusions are presented in Section 6.

Throughout this paper we use a cosmology with $H_0 = 70$ km $s^{-1} Mpc^{-1}$, $\Omega_m = 0.3$ and $\Omega_\Lambda = 0.7$. This gives a luminosity distance to 3C 305 of 184 Mpc and an angular scale of 0.821 kpc $arcsec^{-1}$.

2 OBSERVATIONS AND DATA REDUCTION

2.1 Radio observations

Deep radio observations of 3C 305 have previously been made with the VLA (H82) and MERLIN (Jackson et al. 2003). Our motivation in making new observations was to obtain a high-resolution, high-frequency view of the polarized and total intensity in order to constrain the properties of the depolarizing medium: the essentially complete depolarization observed across broad regions of the source by H82 implies a significant Faraday-active medium but only gives limits on its properties. We therefore observed 3C 305

Table 1. Observations of 3C 305 with the VLA

Date	Config	Frequencies (GHz)	Time on source (h)
2008-Oct-26	A	22.135, 22.535	2.6
		8.435, 8.735	2.0
2009-Apr-14	B	22.135, 22.535	2.6
		8.435, 8.735	2.0
2009-Jul-03	C	22.135, 22.535	2.8

with the VLA (proposal ID AH982) at frequencies around 8.6 GHz (X-band) and 22.3 GHz (K-band), the highest pair of frequencies that would give adequate sensitivity at the time of the proposal, using several VLA configurations; observational details are given in Table 1. All observations used two observing frequencies each with 50 MHz bandwidth (the two frequencies used are given in Table 1). For both observations, we used primary referenced pointing to obtain the best possible pointing accuracy of the array – this is particularly important at K-band where the primary beam of the VLA is small (FWHP 2 arcmin). For the K-band observations we used fast-switching mode to nod between the target and a nearby calibrator, 1436+636, 1.4° from the target, on a timescale of 100 s (70 s on source, 30 s on calibrator). This allows accurate tracking of the rapidly varying atmospheric phases at K-band. The short baselines provided by the more compact configurations of the VLA (the shortest baseline at both bands is ~ 6 k λ , corresponding to an angular scale of 30 arcsec) means that the whole source (LAS = 13 arcsec) is adequately sampled.

All observations were reduced in AIPS in the standard manner. Polarization calibration was carried out using 3C 286 as a reference source. After initial imaging, we carried out several iterations of phase self-calibration on all but the 22.3-GHz A-configuration data (where the signal-to-noise was too low to give a significant improvement over the already good phases provided by fast switching). After phase self-calibration and cross-calibration to ensure that phases were aligned, the *uv* datasets were concatenated for imaging.

Imaging was carried out in AIPS using suitable tapering and weights to obtain appropriate resolutions. Our final imaging products were a full-resolution K-band image (resolution 89×84 mas; rms noise $32 \mu\text{Jy beam}^{-1}$ in all three Stokes parameters), shown in Fig. 1, and matched-resolution, matched-shortest-baseline X- and K-band images (resolution 0.2×0.2 arcsec; rms noise $17 \mu\text{Jy beam}^{-1}$ at X-band and $23 \mu\text{Jy beam}^{-1}$ at K-band), which are shown in Fig. 2.

We also obtained the L-band (1.4 GHz) MERLIN observations of Jackson et al. (2003) from the MERLIN archive, using the standard archive processing, and re-processed a short archival A-configuration L-band VLA observation, with the aim of searching for any polarization at L-band. We do not present any images from these data (which are the basis of the 3CRR Atlas¹ images used by M09) but comment on their implications for depolarization in Section 3.2.

2.2 Chandra observations

3C 305 was observed with *Chandra* for 8 ks in 2008 (M09); our two new observations were taken in early 2011. All three observations used the ACIS-S instrument in VFaint mode with the radio

Table 2. *Chandra* observations of 3C 305

Date	Obsid	Livetime
2008 Apr 07	9330	8218
2011 Jan 03	12797	28661
2011 Jan 06	13211	28661

galaxy lying at the aim point on the back-illuminated S3 chip. Observational details are given in Table 2. There were no periods of significantly high background, and so the livetimes quoted are unfiltered. All three observations were reprocessed using CIAO 4.3 and CALDB 4.4.5 in the standard manner to apply the latest calibration and to apply ‘VFaint cleaning’ to reduce the cosmic-ray background.

For imaging, we used the CIAO *merge_all* script to produce a merged events file in the energy range 0.5–5.0 keV, with a total exposure time of 65.5 ks. We generate images from this events file by binning: as the best estimates of the arrival positions of individual photons have sub-pixel accuracies, due to the multi-pixel nature of event reconstruction and the dithering of the spacecraft, we generally use sub-pixel binning and smoothing to produce the best images.

In our spectral analysis, we extracted spectra in the standard manner using the CIAO *specextract* script. Spectra from each individual observation, and their associated response files, were merged using the *combine_spectra* contributed tool before fitting, as this makes the best use of the data when, as in this case, the dataset is broken up into several small pieces. The merged spectra were then binned so as to have a minimum of 20 counts per bin after background subtraction, and spectral fitting was carried out in XSPEC 12. For all our spectral fitting we assumed a Galactic column density of hydrogen, $N_{\text{H}} = 1.69 \times 10^{20} \text{ cm}^{-2}$, as given by the online COLDEN² tool. Fits were carried out in the energy range 0.4–7.0 keV and errors quoted are 1σ for one interesting parameter.

Accurate astrometric alignment of the X-ray and radio data is difficult. Unusually for a radio galaxy of this luminosity, 3C 305 shows no central unresolved radio component; the brightest central feature of the radio maps is resolved, strongly polarized and steep-spectrum (as noted by Jackson et al. 2003, and see Fig. 2) and so it is not appropriate to align the maps on this feature. There is also no clear unresolved central point source in the *Chandra* data, suggesting that any AGN- or jet-related X-ray emission is weak (as previously discussed by Evans et al. 2009). If we consider only the hard X-ray emission from the source (> 4 keV), which might provide a clue to the location of a heavily absorbed central AGN, we find that there is a significant detection of the central parts of the X-ray emission, whose centroid with the default astrometry is located just at the base of the brightest radio emission, though as there are only 17 counts in a 1-arcsec source circle in the combined image above 4 keV the errors in this position are necessarily large. With this caveat, given that the centroid of these counts lies in a very plausible position for the hidden AGN, we use the default astrometry to relate the X-ray and radio images. This is slightly different from the approach taken by M09, because we have enough hard counts to at least tentatively locate the AGN by this method and because we do not attempt to align on the base of the jet.

An overlay of the radio and X-ray images, showing the key features of the X-ray data, is shown in Fig. 3.

¹ <http://www.jb.man.ac.uk/atlas/>

² <http://xc.harvard.edu/toolkit/colden.jsp>

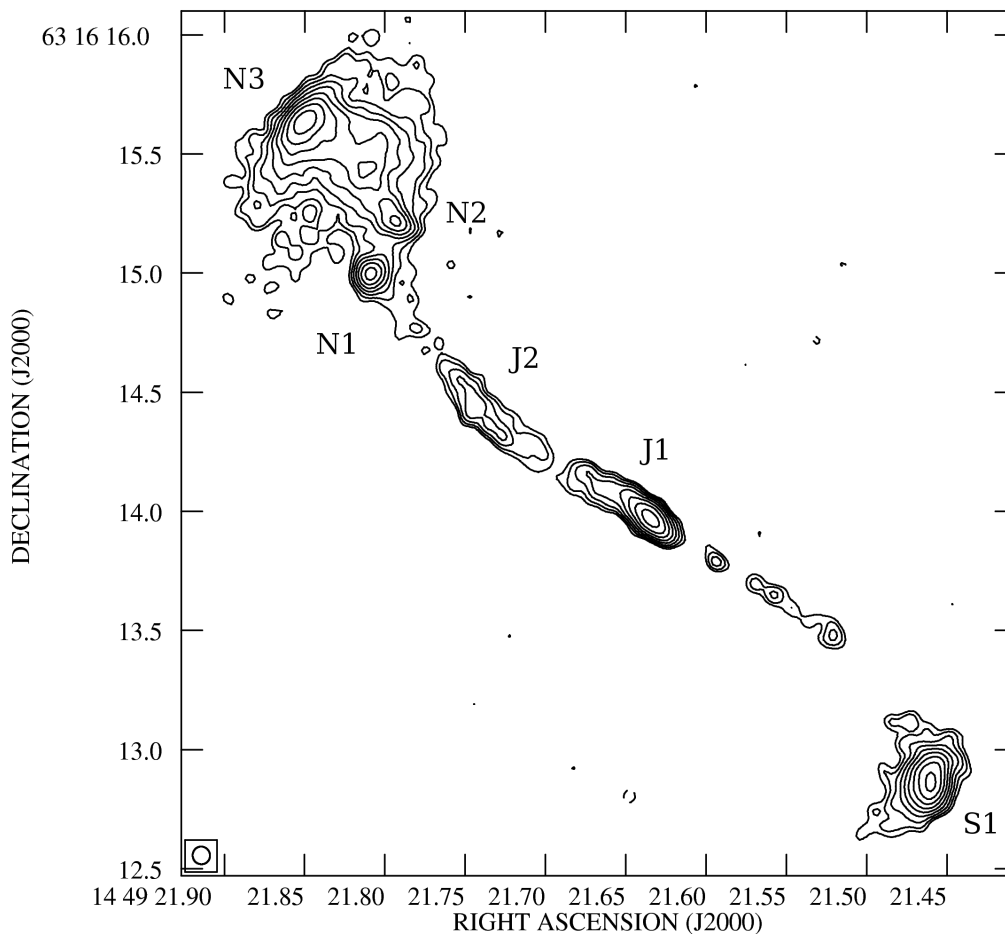


Figure 1. Full-resolution (89×84 mas) total-intensity image of 3C 305 at K-band (22.3 GHz). Contours start at the 4σ level as given in the text and increase by a factor $\sqrt{2}$ at each step. Features discussed in the text are labelled. The distance from hotspot to hotspot (peak of N3 to peak of S1) is 3.9 arcsec (3.2 kpc).

2.3 Other data

We also make use of the *Hubble Space Telescope* (*HST*) continuum-subtracted image of the 500.7 nm [OIII] line, originally presented by Privoon et al. (2008) and also used by M09; this image’s astrometry was corrected by M09 to align the peak of the [OIII] emission with the base of the jet in the radio map, and we adopt this alignment in the absence of any more accurate location of the AGN in either map. The relationship between the [OIII] and X-ray emission is shown in Fig. 4. It can be seen that there is not a one-to-one correspondence between the X-ray and [OIII] emission, though there are many features in common. The X-ray emission appears more similar to the image of $H\alpha + [NII]$ presented by H82 (their fig. 4).

3 RADIO RESULTS

3.1 Total intensity

Our lower-resolution images (Fig. 2) show the structure of the source well and give a very similar picture to that observed in earlier VLA and MERLIN imaging (H82; Jackson et al. 2003). Like many low-redshift radio galaxies, 3C 305 has obvious bright jets and hotspots, but, unlike most, it has low-surface brightness, steep-spectrum regions that extend perpendicular to the source on either side of the jet. These regions (which we will refer to as the lobes, in

spite of their unusual morphology) are strongly polarized with the magnetic field vector pointing down the surface brightness gradient (i.e. perpendicular to the jet).

The jet is well resolved at the full K-band resolution (Fig. 1) and clearly shows a slight S-shape in both jet and counterjet, with edge-brightening at the outer edges of curves (J1, J2). A bright knot at the end of the jet, N1, is the most compact feature in the hotspot region, and would be described as the primary hotspot by the criteria of Hardcastle et al. (1997), meaning that the brightest part of the NE lobe (N2, N3, and the bright emission around them) is likely to be a secondary hotspot complex characterized by repeated redirection of the jet flow. This is consistent with the fact that N1, N2 and N3 are all elongated perpendicular to the presumed local jet direction. By contrast, there is only a single compact feature, S1, in the SW lobe, again clearly elongated perpendicular to the jet direction.

3.2 Polarization

As first noted by H82 there are regions of strong depolarization close to the jet axis in the lobes and hotspots of 3C 305. Our 8-GHz image, though made with very much better sensitivity and resolution, shows very similar polarization properties to the 5-GHz image presented by H82, including regions where little or no polarization is detected (Fig. 2). At 22.3 GHz, though, almost all of

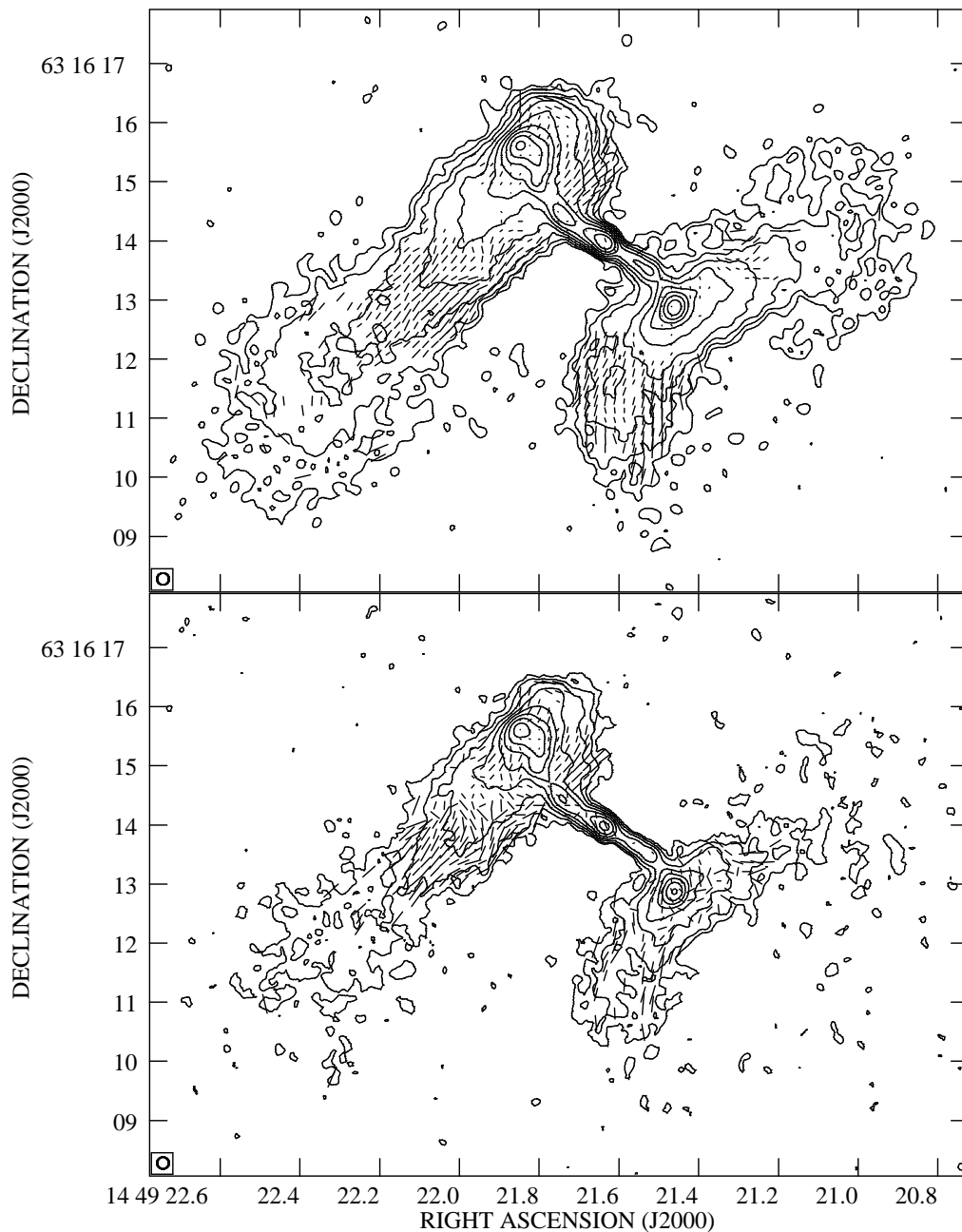


Figure 2. Matched-resolution VLA images of 3C 305 at (top panel) X-band (8.6 GHz) and (bottom panel) K-band (22.3 GHz). Contours start at the 3σ level, as given in the text, and increase by a factor 2 at each step. Polarization vectors are plotted at 90° to the E-vector direction, and their length shows relative fractional polarization. Vectors are only plotted where the signal in both polarization and total intensity exceeds the 3σ level.

the bright regions of the source are strongly polarized, as we would expect for the hotspot regions of a radio galaxy. This frequency dependence, in maps of matched spatial resolution, rules out simple beam depolarization, where the depolarization arises because we are averaging over unresolved complex polarization structure.

Because we see repolarization at high frequencies we can characterize the depolarization quantitatively. We calculate the quantity DP_8^{22} , defined as the ratio of the fractional polarization at 8.6 GHz to that at 22.3 GHz, at each pixel in the map where the total intensity at both 8.6 and 22.3 GHz exceeds the 4σ level and where the polarized intensity at 22.3 GHz also exceeds the 4σ level.

Where there is no detected polarization at 8.6 GHz in a pixel that satisfies these criteria, we replace the 8.6-GHz polarization with its 4σ upper limit so that the depolarization can be easily visualised. The resulting map of DP_8^{22} , with overlaid [OIII] and X-ray contours, is shown in Fig. 5. This image has several interesting features. First, we note that the depolarization is at very similar levels in the NE and SW lobes: since there are several arguments (Jackson et al. 2003) that the source is at a non-negligible angle to the line of sight, this gives an indication that any depolarizing medium must be closely associated with the direction of the radio jet rather than being an unrelated foreground feature in the galaxy, since otherwise

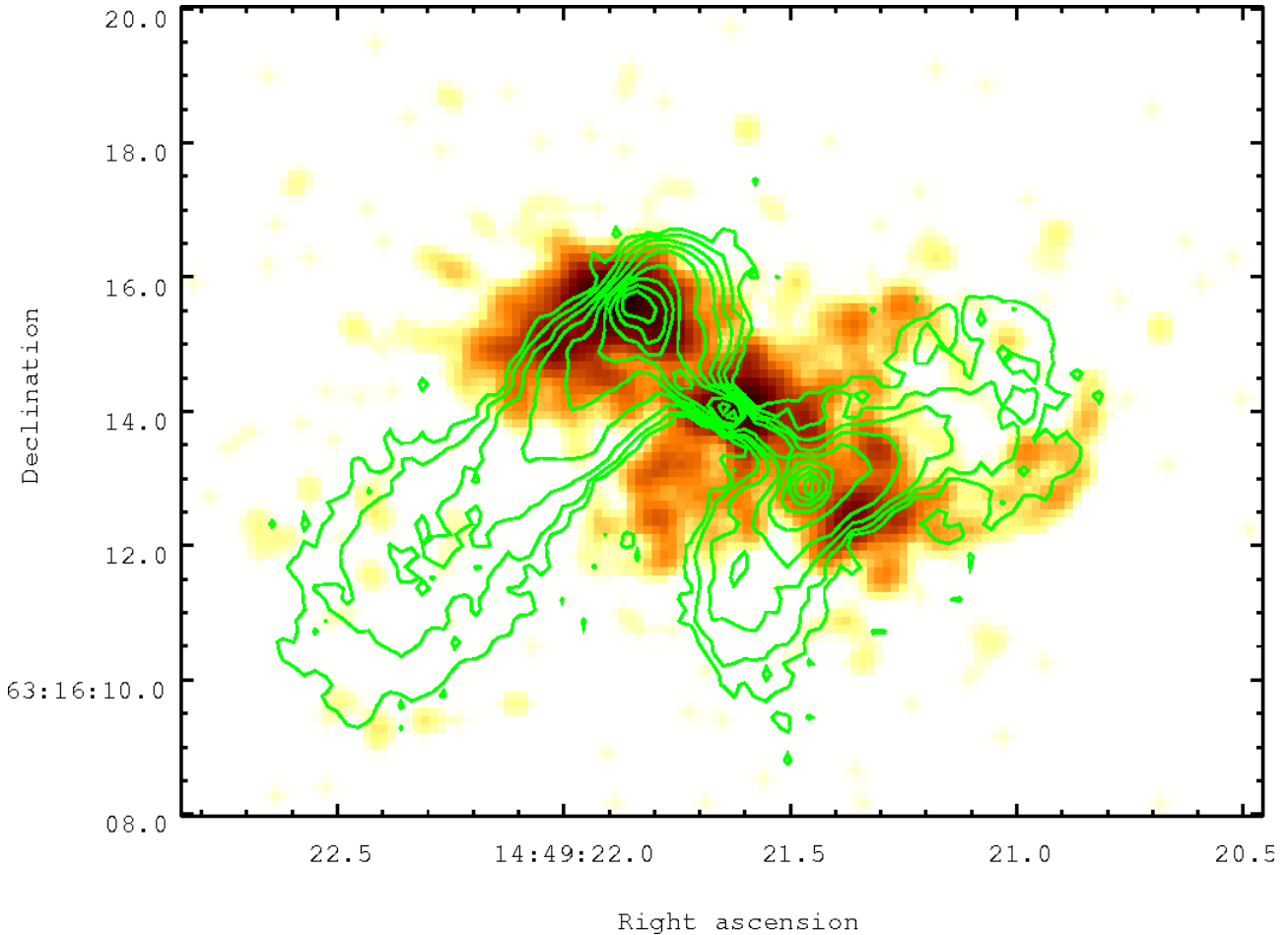


Figure 3. Radio and X-ray image of 3C 305. Contours are from the 8-GHz image of Fig. 2. The colours show the *Chandra* data in the 0.5–5.0 keV band, binned in pixels of 0.123 arcsec on a side and smoothed with a Gaussian of FWHM 3 pixels; the smoothed *Chandra* image has an effective resolution of ~ 0.6 arcsec.

we would expect to see a jet/counterjet side asymmetry along the lines of the well-known Laing–Garrington effect (Laing 1988; Garrington et al. 1998). Secondly, we see strong, resolved variations in DP even in the depolarized regions (especially when we bear in mind that in some cases we are only measuring an upper limit on DP): although some of this may be attributable to differences in the geometry of the depolarizing medium or to different intrinsic polarizations at different frequencies, it seems most likely that the depolarizing medium must be clumpy on scales of ~ 0.5 arcsec (0.4 kpc). Thirdly, we see that in the NE lobe the edges of the depolarization region are quite clearly delineated – the lobe to the NW and SE of the jet has $DP \sim 1$ – and that these edges are not parallel to the jet direction. The depolarization silhouette within the lobe is only 0.8 arcsec (0.7 kpc) wide at the innermost point at which this can be measured, compared to 2.0 arcsec (1.6 kpc) at its outermost point. We cannot say definitively whether this is so in the SW lobe because the NW edge of this feature is not very well detected at 22.3 GHz, presumably due to its steep radio spectrum, but there are hints that the depolarization is lower on the NW edge. Finally, we note that the depolarization seems to be considerably better associated with the X-ray emission than with the emission-line gas as traced by the [OIII] image – in particular, all depolarized parts of the source are coincident with bright X-ray emission, while there is a region in the NE lobe where there is strong depolarization but little or no [OIII] emission. All of these features, taken together, are

qualitatively very consistent with the idea that the depolarization is due to a Faraday screen, closely associated with but external to the jets and lobes, and which either is the X-ray-emitting gas itself or is distributed in a very similar way. We will test this idea more quantitatively in the following sections.

Finally, we note that no polarized emission is seen from the L-band (1.4 GHz) MERLIN observations, and almost none from the A-configuration L-band VLA data – there is a weak detection of polarization from the NW edge of the NE lobe, corresponding to the region in Fig. 5 where $DP_8^{22} \approx 1$. As the outer parts of the lobes are strongly and uniformly polarized at 8 GHz, this suggests that there is some Faraday-active medium on larger scales than the observed X-ray emission.

4 X-RAY RESULTS

4.1 Imaging

As seen in Fig. 3, and as previously noted by M09, the X-ray emission is morphologically different from the radio emission and extended on a slightly larger scale. We detect the bright features associated with the core or inner jet and peaking just outside the two radio-bright hotspots, but our much deeper X-ray images (we see 1080 ± 30 0.5–5.0 keV net counts in a 15-arcsec source circle) reveal lower-surface-brightness diffuse emission lying between the

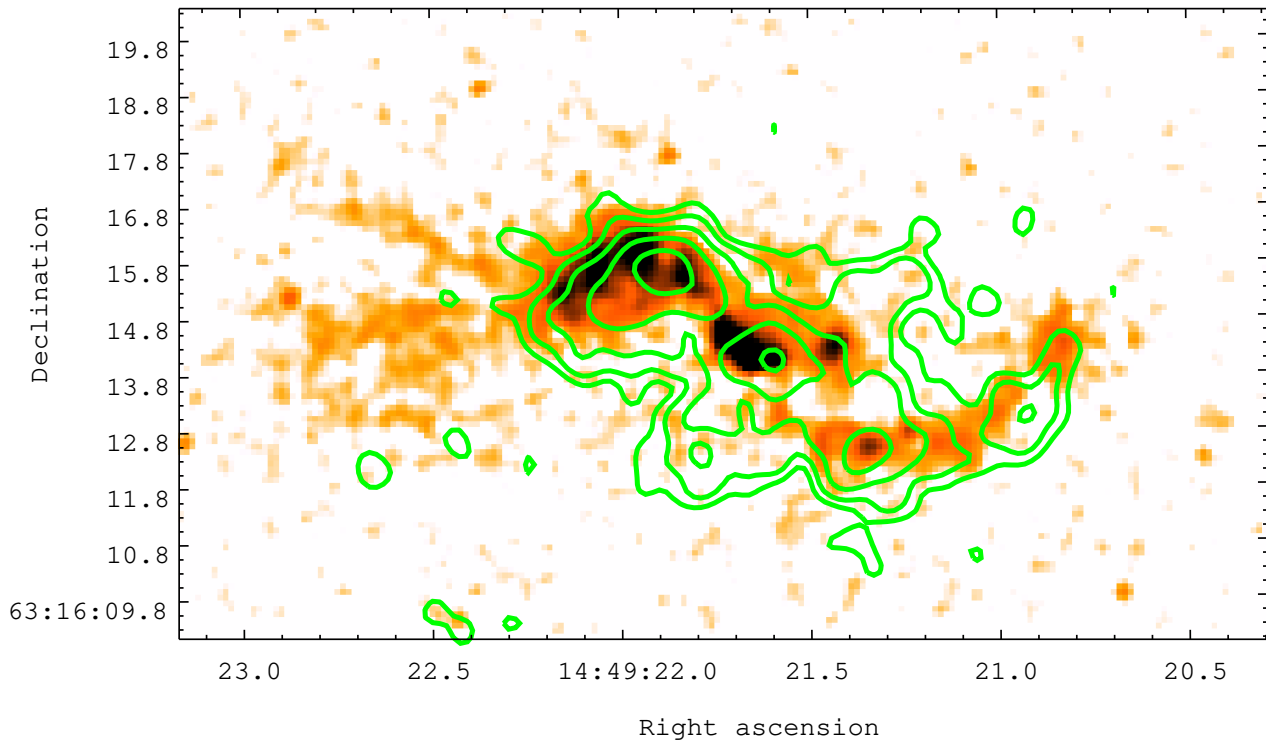


Figure 4. [OIII] and X-ray image of 3C 305. Contours show the 0.5-5.0 keV X-ray emission, binned and smoothed as in Fig. 3: the lowest contour is the 3σ surface-brightness level, calculated using the method of Hardcastle (2000), relative to the off-source background, and each successive contour is a factor 2 higher in surface brightness. The colours show the [OIII] 500.7-nm image of Privon et al. (2008), smoothed with a Gaussian of FWHM 2 pixels to improve surface-brightness sensitivity.

two lobes (the ‘wings’) and just outside the SW lobe (the ‘ridge’). There is a striking similarity to the [OIII] emission in many places, for example in the ridge (Fig. 4), but also some differences: in particular, the ‘wings’ between the two lobes have no [OIII] counterpart in the *HST* images, although, as noted above, there may be some corresponding $H\alpha$ + [NII] emission in the ground-based images of H82. Similar X-ray and $H\alpha$ extension perpendicular to the jets, though on a larger physical scale, was seen in our observations of 3C 171.

We find no evidence for the larger-scale X-ray emission (beyond 15 arcsec, or 12 kpc, from the core) that would be expected if 3C 305 lay in a cluster or group of galaxies. We estimate a total of 90 ± 70 0.5-5.0 keV counts in an annulus between 15 arcsec and the edge of the S3 chip, at 1.5 arcmin (73 kpc); this corresponds to a 3σ upper limit on bolometric luminosity around 10^{41} erg s^{-1} (for $kT = 1$ keV, abundance 0.3 solar), which is well below the total luminosities of typical groups (e.g. Osmond & Ponman 2004) and, as will be seen below, considerably lower than the luminosity of the extended X-ray emission within 15 arcsec. As IC 1065 is a low-redshift galaxy located in the part of the sky covered by the Sloan Digital Sky Survey (SDSS), we searched, using the NASA Extragalactic Database (NED) for any other galaxies within a projected radius of 1 Mpc (≈ 20 arcmin) and ± 1000 km s^{-1} in velocity of 3C 305, and found only three for which NED has redshifts, of which the nearest (and brightest) is the spiral MCG +11-18-009, 130 kpc away in projection and 1.5 magnitudes fainter; the remaining two are so far away that it seems unlikely they are physically associated with IC 1065. It thus certainly seems plausible that 3C 305’s host, though a massive galaxy (H82) lies in a very poor environment, explaining the lack of group-scale X-ray emission:

similar conclusions based on targeted optical spectroscopy were reached by Miller et al. (2002). 3C 305 thus differs from FRI radio galaxies of comparable radio power (e.g. 3C 66B, 3C 442A, M87, 3C 465) which lie in rich groups or clusters (Croston et al. 2003; Hardcastle et al. 2007; Böhringer et al. 1995; Hardcastle, Sakelliou & Worrall 2005) and also from at least some low-power FRII sources (e.g. 3C 285, which lies in a poor to moderate group: Hardcastle et al. 2007).

There is also no evidence for any emission spatially associated with compact features of the radio galaxy such as the jets or hotspots. Synchrotron emission is known from a large number of hotspots and jets in low-power radio galaxies of this type, but none is apparent in 3C 305.

4.2 Spectral fits

Spectra were extracted, in the manner described in Section 2.2, for the following regions:

- (i) ‘Core’: a 1.4-arcsec circle centred on 14:49:21.618, +63:16:13.90, which is the approximate centroid of the hard X-ray emission discussed above and also lies just to the SW of the base of the radio jet.
- (ii) ‘Whole source’: a 15-arcsec circle with the same centre, encompassing all of the emission plausibly associated with the source.
- (iii) ‘Extended’: the whole source minus the core region.
- (iv) ‘Hotspot’: the bright region of X-ray emission around and to the NE of the NE radio hotspot, defined as an elliptical region with semi-major axis 2.3 arcsec, semi-minor axis 1.6 arcsec, and

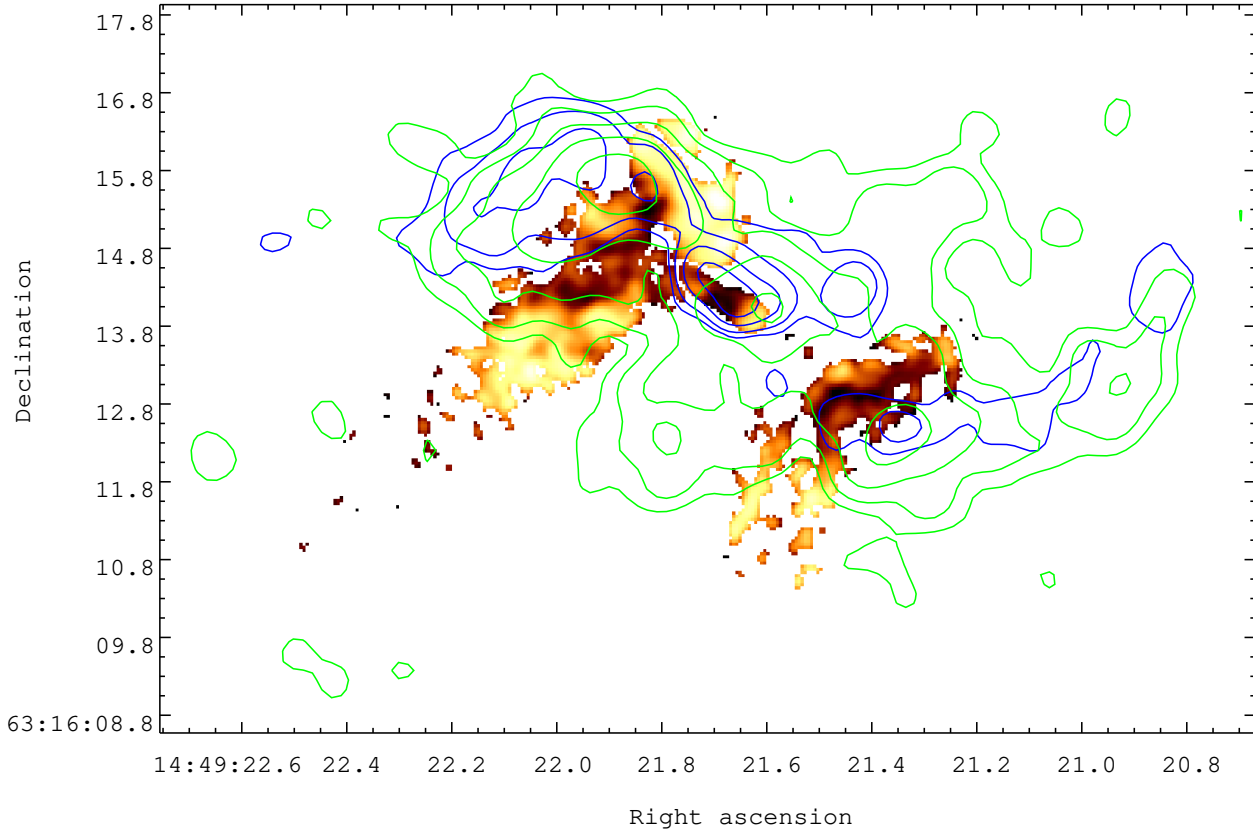


Figure 5. A map of the depolarization measure DP_8^{22} between 22.3 and 8.6 GHz, as described in the text. Overlaid are contours of the X-ray emission (green, as in Fig. 4) and the smoothed [OIII] emission from Fig. 4 (blue). Black regions have $DP < 0.1$ (highly depolarized), red-orange have $0.1 < DP < 0.5$ (moderately depolarized) and yellow-white regions show little or no depolarization ($0.5 < DP \lesssim 1$).

position angle 35° (north through east) centred at 14:49:21.937, +63:16:15.29: this region was selected because it is the brightest sub-region of the X-ray emission and is coincident with the clearest depolarization silhouette. (Note that, while roughly coincident with the radio hotspot, this region is much larger than the hotspot and is not, as noted above, associated with any detected non-thermal emission.)

(v) ‘Wings’: the extended emission elongated roughly perpendicular to the jet axis across the centre of the source, enclosed by an elliptical region with semi-major axis 3.8 arcsec, semi-minor axes 1.3 arcsec, and excluding the core region.

The locations of the core, hotspot and wings regions are shown in Fig. 6. For all these regions the background was taken to be an annulus between 15 and 20 arcsec concentric with the core, which contains no detected point-like or extended emission. We did not attempt to take local background for sub-regions of the source because of the non-uniformity of the extended emission.

Simple power-law models were not an acceptable fit to any of the extracted spectra (the lowest reduced χ^2 value, 3.4, was found in the core region). All of the spectra had the characteristic excess between 0.7 and 1.1 keV that is typical of emission from keV-temperature partially ionized gas. Accordingly, we next fitted with single Astrophysical Plasma Emission Code (APEC) models with free abundance relative to solar and temperature; these models accurately represent the continuum and line emission from a colli-

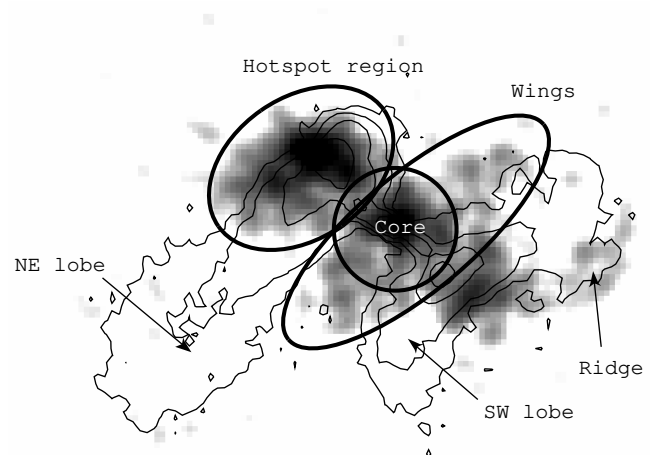


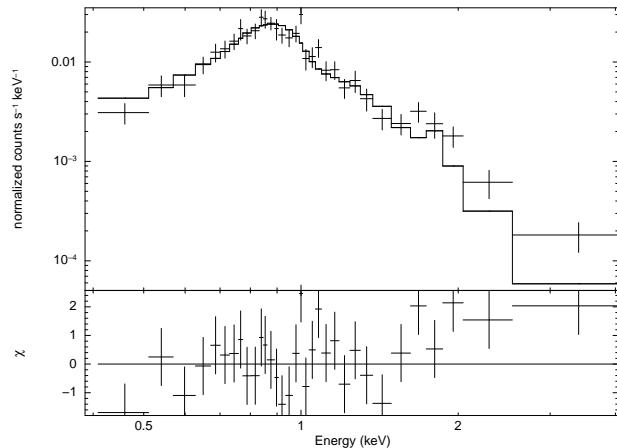
Figure 6. Locations of the core and hotspot X-ray extraction regions. The ‘Whole source’ region encompasses all the emission seen here. Grayscale shows the X-ray emission binned and smoothed as in Fig. 3. Contours are from the 8.4-GHz radio map at $3\sigma \times (1, 4, 16, \dots)$ mJy beam $^{-1}$.

sionally ionized plasma³. Results of these fits are given in Table 3 and an example X-ray spectrum is shown in Fig. 7.

³ See <http://atomdb.org/>

Table 3. Net counts from, and APEC fits to the spectra of various regions of 3C 305 and the corresponding bolometric X-ray luminosities of the thermal component.

Region	Net counts (0.5-5.0 keV)	χ^2/dof	kT (keV)	Abundance (solar)	$L_{\text{Bol, unabs}}$ ($\times 10^{41}$ erg s $^{-1}$)
Core	255 \pm 16	31.3/8	1.02	0.10	–
Whole source	1091 \pm 35	78.2/41	0.81 \pm 0.02	0.15 \pm 0.02	4.8 \pm 0.5
Extended	836 \pm 32	40.6/33	0.78 \pm 0.02	0.15 \pm 0.03	3.9 \pm 0.4
Hotspot	384 \pm 20	19.4/13	0.80 \pm 0.03	0.20 \pm 0.05	1.7 \pm 0.3
Wings	112 \pm 11	6.1/5	0.97 \pm 0.10	0.12 $^{+0.08}_{-0.05}$	0.6 \pm 0.1


Figure 7. X-ray count spectrum, fitted model and contributions to χ^2 for the ‘Extended’ region discussed in the text.

From this table it can be seen that the single-APEC fits to the extended region, wings and hotspot are acceptable but the fit to the core is very clearly not, and the fit to the whole source is similarly rather poor (reduced $\chi^2 \sim 2$). This is not unexpected if the hard counts noted above come from the location of an absorbed AGN. We therefore fitted a model to the core spectrum consisting of an APEC plus an intrinsically absorbed power law. The absorbing column, photon index and normalization of the power law were free to vary: the abundance of the APEC component was set to 0.2 solar, based on what is found in the free-abundance fits, to reduce the number of free parameters. This model was a good fit ($\chi^2/\text{dof} = 1.7/6$) with $kT = 0.73 \pm 0.06$, photon index $\Gamma = 1.7 \pm 0.5$ and intrinsic absorption column $3^{+5}_{-2} \times 10^{21}$ cm $^{-2}$. The photon index is consistent with what is seen in the absorbed components of narrow-line radio galaxies (e.g. Hardcastle, Evans & Croston 2009). (The implications of this model for the X-ray emission of the AGN are discussed in Section 5.1.)

We then took this best-fitting model for the power-law component of the core, with all parameters frozen, and added it to the APEC model fitted to the whole source; we found that, as might be expected, the fit was much improved ($\chi^2/\text{dof} = 52.8/41$, $kT = 0.78 \pm 0.02$, abundance 0.18 ± 0.03). Thus it is reasonably clear that the extended emission can adequately be fitted with a model in which it originates in a single-temperature, thermal, collisionally ionized plasma (though our data are not good enough to rule out multi-temperature models). The unabsorbed luminosity in the thermal component of this X-ray emission is 1.8×10^{40} erg s $^{-1}$ (2-10 keV rest-frame) or 4.4×10^{41} erg s $^{-1}$ (bolometric). This is much lower than the estimated line luminosity of the system, $\sim 10^{44}$ erg s $^{-1}$ (H82); we return to this point below (Section 5.4).

The low best-fitting abundances in the APEC fits are noteworthy. Abundances in the hot phase of the ISM/IGM in groups of

galaxies, which are the most obvious comparison to 3C 305, tend to be significantly higher than our best-fitting values, particularly at the centres of the host groups (e.g. Johnson et al. 2011). There are several possible explanations for our results. One is that this is a real effect: it might, for example, arise if the hot gas comes from a recent interaction between the radio galaxy and low-abundance cold gas, as we will argue in Section 6. However, low abundances can also be an artefact of fitting the wrong model: if a single-temperature model is fitted to a two-temperature plasma, the abundance is systematically low (Buote & Fabian 1998) while a similar effect might be expected if the plasma is photoionized rather than collisionally ionized (see Section 5.2). We cannot rule out these explanations from the X-ray spectroscopy alone.

Finally, we note that the consistency between the APEC parameters estimated for the hotspot, wings and the whole extended region, and the good fits obtained with Galactic N_{H} values, suggests that there is no significant effect of spatially variable intrinsic X-ray absorption on the X-ray spectrum. The deep, narrow component of HI ($N_{\text{HI}} = 5.4 \times 10^{20}$ cm $^{-2}$) observed by Morganti et al. (2005a) is in front of the SW lobe, and there is relatively little X-ray emission there (Fig. 3), though the statistics are not good enough to say whether this is an effect of absorption. The broad, shallow component corresponds to a higher column density ($N_{\text{HI}} = 2 \times 10^{21}$ cm $^{-2}$ for an assumed spin temperature of 1000 K) and Morganti et al. place this in front of the NE radio lobe, where the bright ‘hotspot’ X-ray emission is seen. Fitting an APEC model with both Galactic and intrinsic absorption to the spectrum from this region, we can place a 99% confidence upper limit on the intrinsic column density of $< 1.5 \times 10^{21}$ cm $^{-2}$ if the temperature and abundance are allowed to vary, and $< 1.1 \times 10^{21}$ cm $^{-2}$ if they are fixed to force consistency with the overall extended spectrum. It seems most likely, therefore, that at least some and quite possibly all of the HI is behind, or mixed in with, some or all of the X-ray emitting gas. In practice, the neutral hydrogen is unlikely to be cleanly separated from the X-ray-emitting plasma: it is more likely that the two form part of a multi-phase medium, together with the warm gas emitting in optical emission lines, with the HI having a comparatively low filling factor (as suggested by O’Dea et al. 1994). In this situation, we would expect a much lower effective absorbing column in X-ray spectroscopy than is observed toward the radio continuum. We also note that a higher spin temperature than assumed by Morganti et al. (2005a), which is perfectly possible in the radiative environment of the AGN (e.g. Liszt 2001; Holt et al. 2006) would increase the discrepancy between the X-ray limit and HI measurements, and would therefore strengthen the argument in favour of a complex multi-phase medium.

4.3 Hardness ratio analysis

An alternative method of searching for any spectral variation as a function of position in the source is to consider hardness ratios.

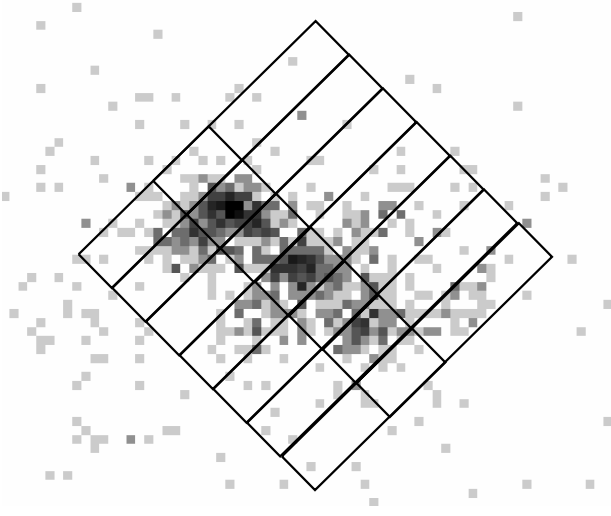


Figure 8. Regions used for hardness ratio extraction

Generically, these are based on the ratio of X-ray fluxes in two bands (‘hard’ and ‘soft’). Their advantages are that they can be calculated in regions where there are too few counts to fit X-ray spectra, and that their interpretation does not pre-suppose any physical model. In general, estimating hardness ratios as a function of position for an extended X-ray source requires some idea of the effective area as a function of position — the flux corresponding to a given number of counts is not constant over the detector. Given the small physical size of 3C 305, though, we can make the simplifying assumption that the energy-dependent effective area is constant over our region of interest. We divide the counts from the source into 3 energy bands, ‘soft’ (0.5 - 1.0 keV), ‘medium’ (1.0 - 2.0 keV) and ‘hard’ (2.0 - 7.0 keV). Then we define hardness ratios as follows:

$$H_1 = 1 + \frac{C_M - C_S}{C_M + C_S}$$

$$H_2 = 1 + \frac{C_H - C_M}{C_H + C_M}$$

where C_S , C_M and C_H are the counts in a given region in the three bands. As the errors on the counts are Poissonian, the errors on these hardness ratios have a distribution that is hard to describe analytically. See Appendix A for a discussion of the approach we adopt.

Rather than replicate the regions used for our spectral analysis, we decided to divide the source up into identically sized rectangular regions along the jet axis. This allowed us to search for spectral variation as a function of distance from the nucleus, which might be expected in photoionization models for the extended X-ray emission. The minimum size of these regions was determined by the requirement that we should obtain enough counts in the hard band to allow a calculation of the hardness ratio. This allowed 7 regions along the jet axis. We centred the middle region on the core, while two of the outer regions more or less coincide with the positions of the radio hotspots. We defined large and small versions of our regions: the large versions contain essentially all the emission from the source, while the small versions are restricted to ± 1.05 arcsec around the jet axis (Fig. 8). We then estimated the hardness ratios H_1 and H_2 in each bin using the method described in Appendix A. The background for this bin size was < 1 count in each bin and so we neglected it. Results are plotted in Fig. 9.

We see that there is little strong evidence of variation of hardness ratio as a function of position, consistent with the spectral analysis presented above. We note first of all that the hardness ratios of both sets of regions are consistent within the joint errors everywhere (this is not surprising, as they are not independent, but it gives an indication that there is no significant difference between the off-axis and on-axis parts of the source). There is a clear central peak in H_2 in both sets of plots, which is not surprising given the overdensity of hard counts in the core region discussed in Section 2.2. There also seems to be a marginally significant deficit of hard counts in the region at ~ -3 arcsec from the core, which corresponds to the peak of the ‘hotspot’ region in our spectral analysis. But other than that, there seems to be no clear evidence for HR variation as a function of position: within the errors, H_1 is consistent with being constant (~ 0.8) throughout the source, while $H_2 \sim 0.3$. This supports our conclusion from spectral analysis that the bulk of the extended emission is adequately represented by a model with a single X-ray spectrum and that there are no strong variations of absorbing column with position in the source.

5 DISCUSSION

5.1 The X-ray core and the state of the AGN

As noted above, the best-fitting absorbed power-law model for the core region gives a spectrum which has properties reasonably similar to those of the nuclei of other narrow-line radio galaxies.

However, the unabsorbed 2-10 keV luminosity of the power-law component in this model is only $(5 \pm 1) \times 10^{40}$ erg s $^{-1}$ (where the error is derived from the 1σ error on normalization only), which is extremely low compared to most 3CRR radio galaxies, and would place 3C 305 an order of magnitude or more below the correlation between radio power and X-ray nuclear power observed for narrow-line radio galaxies (Hardcastle et al. 2009). Given that few NLRG have a column density $< 10^{22}$ cm $^{-2}$ towards the heavily absorbed component, it may be that we are seeing absorption towards only the jet-related component, and that the accretion disc is behind a much larger column, although we note that, since there is only an upper limit on the compact radio core flux, we would not expect a strong jet-related component either (see Hardcastle et al. 2009 and references therein). Jackson et al. (2003) suggest that the optical nuclear component is consistent with being a reddened quasar with $A_V > 4$, but this only requires $N_H \gtrsim 7 \times 10^{21}$ cm $^{-2}$, consistent with our best-fitting model. However, the estimate given by Jackson et al. of the M_V of the hidden quasar, -22.5 , would lead us to expect a much more luminous X-ray source (e.g. Elvis et al. 1994), requiring a much higher obscuring column. The *Spitzer* 24- μ m flux quoted by Dicken et al. (2010) implies that $L_{\text{IR}} \sim 2 \times 10^{43}$ erg s $^{-1}$, which, on the correlation between L_{IR} and accretion-related X-ray reported by Hardcastle et al. (2009), would lead us to expect a nuclear X-ray luminosity $\sim 10^{43}$ erg s $^{-1}$. Finally, we could estimate the nuclear X-ray luminosity from the [OIII] luminosity, using the correlation of Heckman et al. (2005), but this relies on the uncertain reddening correction, as well as on the excitation mechanism for the [OIII]; if we do not correct the H82 [OIII] fluxes for reddening (see the discussion of this point in Section 5.4), we would again obtain an expected 2-10 keV luminosity around 10^{43} erg s $^{-1}$, but this could be substantially lower if the emission-line regions are partially or wholly shock-excited, or substantially higher if the reddening correction is large, making such estimates very uncertain.

All these data are difficult to reconcile. One obvious explanation is that the source has varied substantially on a timescale of

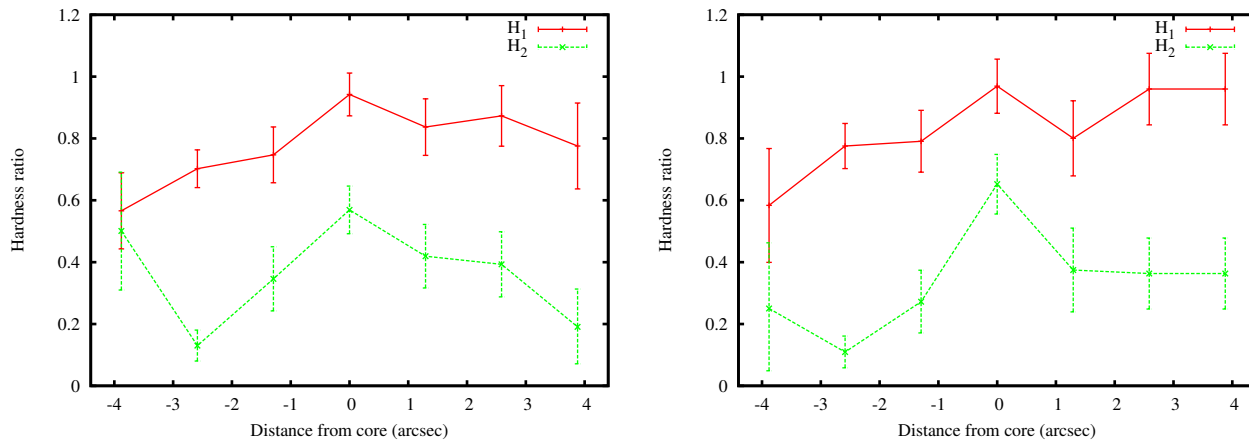


Figure 9. Bayesian estimates (see Appendix A) of the hardness ratios, as defined in the text, as a function of position for (left) large and (right) small bins positioned along the jet axis as shown in Fig. 8. Distances are defined along the jet axis, relative to the core, and increase in the direction from NE to SW.

years to decades, although there is no evidence for this in our multi-epoch X-ray data or in the *XMM-Newton* data studied by Evans et al. (2008). There would be a significant time lag between a substantial drop in the optical/X-ray output of the accretion disc and the corresponding drop in the luminosity of re-radiated emission from the ‘torus’ region, which could help to explain the difference between the X-ray and IR luminosities. Alternatively, it may be that the AGN is Compton-thick, and that the intrinsic X-ray luminosity currently is roughly the $\sim 10^{43}$ erg s $^{-1}$ implied by the mid-IR data.

5.2 Ionization mechanism

M09 raised the important question: what is the ionization mechanism of the X-ray-emitting gas? Although we obtain good fits with a thermal (APEC) model, implying consistency with a collisional-ionization scenario, we cannot rule out photoionization directly from the *Chandra* spectra. M09 pointed out that the ratio between the [OIII] flux and the soft X-ray flux was of order unity (compare our bolometric X-ray luminosity of 4.4×10^{41} erg s $^{-1}$ with the [OIII] luminosity, calculated from the flux quoted by M09, of 1.5×10^{41} erg s $^{-1}$), which is often observed in Seyfert galaxies, where the X-ray-emitting medium is thought to be directly photoionized by the AGN (e.g. Bianchi et al. 2006). However, in 3C 305, there is reasonably strong circumstantial evidence that the emission lines are shock-ionized, as discussed by H82, and also some direct evidence for this (the detection of [FeII] emission at the likely location of the strongest shocks, Jackson et al. 2003). Any agreement between the luminosities in X-rays and [OIII] may therefore be coincidental, or at least be a reflection of the fact that the same jet is driving both. There are also some practical difficulties with a photoionization model for the X-rays, including the fact that we see no direct evidence in the X-ray for a luminous AGN at all (Section 5.1) let alone one with the luminosity needed to drive the observed extended X-ray emission. Perhaps the strongest argument against photoionization is morphological: in addition to the fact that the apparent association between the radio source and the X-ray emission would have to be a coincidence in such a model, several features of the extended X-rays not seen in the data of M09, such as the ‘wings’ in the centre of the source and the ridge at the edge of the SW lobe, are very hard to reconcile with the expected roughly conical morphology for photoionization, and yet have X-

ray spectra and hardness ratios completely consistent with those of the rest of the source.

To investigate a photoionization model quantitatively we follow the analysis in H10, which was itself based on the analysis of X-ray photoionization in a Seyfert galaxy by Weaver et al. (1995). Consider the entire ‘hotspot’ region to be photoionized by a hidden AGN and, for simplicity (and also because it minimizes the distance of the hotspot from the AGN and so makes the energetic requirements as low as possible) suppose that the X-ray structure lies in the plane of the sky. Then the ‘hotspot’ region can be modelled as a uniformly filled cone between two radii, centered on the AGN, of r_{in} and r_{out} , which we measure to be roughly 2.6 and 6.4 kpc respectively. The opening angle of the cone is 67 degrees, which means that we need to take the curvature of the volume elements into account, so our analysis is slightly different from that of H10. The surface brightness of the hotspot region is roughly constant, with no sign of a strong gradient away from the nucleus, so let the density be given by $n(r) = n_{\text{in}}(r/r_{\text{in}})^{-2}$, so as to keep the ionization parameter constant: then

$$L_{\text{line}} = \int_{r_{\text{in}}}^{r_{\text{out}}} \Omega r^2 n^2(r) j(\xi) dr \quad (1)$$

where Ω is the solid angle subtended by the cone ($\Omega = 2\pi(1 - \cos\theta)$) where θ is the half-opening angle: thus in this case $\Omega = 1.04$ sr) and $j(\xi)$ is the volume emissivity for a given ionization parameter. This gives us

$$L_{\text{line}} = \Omega n_{\text{in}}^2 r_{\text{in}}^4 j(\xi) \left[\frac{1}{r_{\text{in}}} - \frac{1}{r_{\text{out}}} \right] \quad (2)$$

and so for given values of r_{in} , r_{out} and Ω , and for a known value of $j(\xi)$ (we follow Weaver et al. and H10 and use $j(\xi) = 10^{-24}$ ergs cm $^{-3}$ s $^{-1}$) the luminosity determines the density throughout the photoionized region. For the observed 0.1–10 keV luminosity of the hotspot region, 1.4×10^{41} erg s $^{-1}$, we have $n(r_{\text{in}}) = 0.66$ cm $^{-3}$ and $n(r_{\text{out}}) = 0.11$ cm $^{-3}$. These densities are not in themselves particularly implausible – they are roughly comparable to the densities estimated, obviously on quite different assumptions, from the APEC model in Section 5.3, and are similar to the results we obtained for the photoionization analysis of 3C 171. However, the requirement that the ionization parameter $\xi = L_{\text{I}}/nr^2 > 100$ erg s $^{-1}$ cm (Weaver et al. 1995) then implies an ionizing luminosity $L_{\text{I}} > 4 \times 10^{45}$ erg s $^{-1}$. Even if we relax the required ionization

parameter by an order of magnitude, we require $L_1 > 4 \times 10^{44}$ erg s^{-1} .

Can this luminosity be supplied by the AGN? As noted above (Section 5.1) our best estimate of the unabsorbed X-ray luminosity of the nucleus is only 5×10^{40} erg s^{-1} : no correction factor for the non-X-ray part of the ionizing continuum (a factor of a few) can make up this discrepancy. However, as further noted above, the X-ray luminosity seems anomalously low for a NLRG given the radio luminosity of the source and the mid-IR luminosity of the nuclear region. If the AGN has the much higher nuclear X-ray luminosity ($L_X \sim 10^{43}$ erg s^{-1}) implied by the mid-IR data, or has had it in the recent past, then the photoionization model is closer to being viable, but still an order of magnitude off even for the very favourable assumptions that we have used. Although our model parameters are approximate (as we noted above, the extended X-ray emission is not very convincingly modelled as a uniformly filled cone) there are no obvious changes that we could make that would produce a very low density and thus reduce the luminosity needed to produce the ionization parameter required for X-ray emission. As in the case of 3C 171, we conclude that a photoionization model for the extended X-ray emission is difficult to sustain, and so in what follows we make use of densities derived from the APEC fits to the X-ray emission.

5.3 Physical conditions in the depolarizing medium

From the normalization of the APEC fit to the ‘hotspot’ region described in Section 4.2, we can estimate the density of X-ray emitting plasma, on the assumption that the hotspot region is a uniformly filled prolate ellipsoid with the dimensions we used for the extraction. This gives an electron density of $(1.9 \pm 0.1) \times 10^{-1}$ cm^{-3} and a pressure of $(4.5 \pm 0.3) \times 10^{-11}$ Pa, or $(4.5 \pm 0.3) \times 10^{-10}$ dyn cm^{-2} . H82 estimate pressures in the emission-line regions in the range $10^{-9} - 10^{-10.5}$ Pa, which is rather higher than what we find here, but comparable at the lower end, so that it is possible that the X-ray-emitting plasma is in rough pressure balance with the line-emitting material. Neither the density nor the temperature of the line-emitting material is well constrained. The minimum energy density in the lobes U_{\min} is of order 3×10^{-11} J m^{-3} (3×10^{-10} erg cm^{-3}), so assuming a fully tangled field the lobe pressures ($p_{\min} = U_{\min}/3$) are significantly less than the pressures in the hotspot region, which may help to explain why the lobe material is driven away from the jet axis. (Consistent with this, the pressure in the ‘wings’ region, if we assume it to be a uniformly filled oblate ellipsoid with the dimensions of the extraction region, is $(1.7 \pm 0.4) \times 10^{-11}$ Pa, very similar within the errors to the minimum lobe pressure; thus it is possible that the ‘wings’ are shocked material that has been driven back towards the centre by the expanding radio lobes.)

The ‘hotspot’ region is presumably responsible for the depolarization silhouette seen in front of the NE hotspot in the radio. Following Hardcastle (2003), we expect the degree of polarization at a given frequency ν to be given by

$$p_\nu = p_i \exp(-C\nu^{-4}) \quad (3)$$

where p_i is the intrinsic degree of polarization and C depends on the physical conditions in the depolarizing medium:

$$C = 2K^2 (n_e B_{\parallel})_f^2 d R c^4 \quad (4)$$

where K is a constant with value 8.12×10^{-3} rad nT^{-1} m kpc^{-1} , $(n_e B_{\parallel})_f^2$ is the dispersion in the product of number density and mag-

netic field strength along the line of sight in units of $nT m^{-3}$, d is the size scale in kpc of the individual depolarizing regions (regions of uniform magnetic field) and R is the line-of-sight depth through the medium in kpc. For the depolarization silhouette we obtain average values of p_ν by integrating polarized and total intensity over the most depolarized region, and we can then solve eq. 3 for C , obtaining $C = 8.5 \times 10^{39}$ Hz⁴. We take $R = 1.3$ kpc (the semi-minor axis of the ellipsoidal region discussed above). We know that d must be much less than the resolution at X-band (8.6 GHz), $d \ll 0.16$ kpc, and as we know there are still some unpolarized regions even at the full K-band resolution, it seems likely that $d < 70$ pc: $d = 70$ pc should give us a limit. If we further assume that the electron density is constant and that the Faraday dispersion comes only from field reversals, then $(B_{\parallel})_f^2 \approx B^2$, and this tells us that $B \gtrsim 1.6$ nT (16 μ G). Following H10, we expect an upper limit to be such that the energy density in the magnetic field is less than that in the gas, i.e.

$$\frac{3}{2} nkT > \frac{B^2}{2\mu_0} \quad (5)$$

and for the densities and temperatures we have determined above, this implies that $B < 10$ nT (100 μ G), which is consistent with the lower limit derived from depolarization, and requires that $d > 2$ pc. We conclude from this that it is very plausible that the X-ray emitting plasma is the depolarizing medium, and that it is magnetized with a magnetic field energy density which is within an order of magnitude or so of the thermal energy density. If the X-ray-emitting material is the depolarizing medium, its filling factor must be close to unity. As in 3C 171, the self-consistency of these calculations gives some support to a model in which the gas is collisionally ionized rather than photoionized.

5.4 Source energetics

We now have what seems likely to be a full picture of the various phases of gas known to be associated with the outflow in 3C 305. We emphasise that we have no direct evidence for outflow in the X-ray-emitting component, but it is very hard to imagine a model in which this component is not moving with the optical line-emitting gas, which is morphologically similar (Section 4.1) and in rough pressure balance (Section 5.3). In what follows we assume that the X-ray, optical line and HI-emitting material are multiple phases of a single outflow. Guillard et al. (2012) have recently shown that the kinematics of the *molecular* hydrogen in 3C 305 (and in several other sources) do not appear to be consistent with those of the HI or the optical emission-line gas, although we note that some of the energy supplied by the jet is likely to go into excitation of the molecular gas. It is possible that the *Spitzer* observations of Guillard et al. did not have the sensitivity to detect rapidly outflowing material; alternatively, it is possible that the molecular gas is actually dissociated by the process that drives the fast outflow, and so shows apparently different kinematics for this reason. In any event, as the molecular material presents what appears to be a somewhat different kinematic behaviour, we neglect this phase in what follows.

In order to calculate the contributions of each phase to the energy budget of the source, we need to know the speed of the outflow. H82 estimated the kinetic energy in the line-emitting gas on the assumption that its speed is the maximum radial velocity seen in the emission lines ($v_r = 260$ km s^{-1}). This is a lower limit, since the jets, which presumably drive the outflow, are not pointing

directly towards us, and in fact given their two-sidedness are probably reasonably close to the plane of the sky, so that v_r is probably significantly less than v . If the splitting and broadening of the optical emission lines near the NE lobe (Morganti et al. 2005a) is due to us observing shocked material on both sides of the source, then the true outflow velocity would have to be *at least* half the difference between the centroids of the two velocity components, which is $\sim 400 \text{ km s}^{-1}$, consistent with the above. Moreover, in some models of the acceleration of emission-line clouds by shocked gas, it is possible for the clouds to be moving significantly slower than the bow shock (O’Dea et al. 2002). However, v_r and the similar velocities estimated from the HI observations (Morganti et al. 2005a) are the only *direct* constraints on velocity that we have.

One approach to determining the true velocities is to estimate the expansion speed from the observed X-ray and radio properties, following H10. If we think the X-ray emission represents shocked external thermal gas, then the pressure in the ‘hotspot’ region is a proxy of the post-shock pressure; the minimum pressure in the large-scale lobes must be equal to or greater than the pressure in the large-scale unshocked gas in which they are embedded. We can then apply the shock pressure relation

$$\frac{p_2}{p_1} = \frac{2\Gamma \mathcal{M}_1^2 + (1 - \Gamma)}{\Gamma + 1} \quad (6)$$

where Γ is the adiabatic index, $5/3$ in this case, with $p_2 = 4.5 \times 10^{-11} \text{ Pa}$ (the pressure in the ‘hotspot’ region) and $p_1 = 1 \times 10^{-11} \text{ Pa}$ (the minimum pressure in the lobes), to find that $\mathcal{M}_1 \sim 2$. Since we also know that $T_2 = 0.8 \text{ keV}$, and

$$\frac{T_2}{T_1} = \frac{[2\Gamma \mathcal{M}_1^2 + (1 - \Gamma)] [\Gamma - 1 + 2/\mathcal{M}_1^2]}{(\Gamma + 1)^2} \quad (7)$$

we find that the unshocked temperature T_1 is 0.4 keV , the sound speed in the medium is 330 km s^{-1} , and the shock speed v_{shock} would be 650 km s^{-1} . The temperature T_1 is certainly plausible for the hot halo of an isolated massive galaxy (see Section 4.1) and the expected undisturbed bolometric X-ray luminosity of such an object, $\sim 10^{41} \text{ erg s}^{-1}$, is not ruled out by our limits on the large-scale emission. If we assume that the emission-line material is moving with the shock, the speed would be consistent with the observed radial velocities if the angle to the plane of the sky θ were 24° ($v_r = v_{\text{shock}} \sin \theta$), which seems reasonable (and is consistent with the estimates of M09 from jet sidedness); if the emission-line clumps are actually slower than the shock speed, this gives a lower limit on θ . Kinetic energies for the outflowing material are a factor $\csc^2(24^\circ) \approx 6$ higher if we assume that the actual outflow speed $v = v_{\text{shock}}$ than if we assume $v = v_r$, and we use this speed in what follows.

Morganti et al. (2005a) estimated a lower limit on the mass of the emission-line material actually associated with the outflow, for one lobe, of $> 2 \times 10^5 M_\odot$; we adopt twice this value to characterize the overall outflow, but this low mass still makes the kinetic energy contribution of this phase quite negligible. We derive a mass estimate of the X-ray-emitting gas from the normalization of the APEC fits to the ‘hotspot’ region, which gives a density as discussed in Section 5.3. If we very roughly assume a uniform density for the X-ray-emitting gas throughout the source, then scaling the mass for the north hotspot region up to the total by the ratio of the emission measures determined from spectral fitting, we estimate that the mass of the X-ray-emitting gas is $7 \times 10^7 M_\odot$ – the systematic error on this estimate is of course large, principally because we do not know the geometry of the emitting region, but is unlikely to exceed a factor ~ 2 . Morganti et al. (2005a) argue that the mass of HI seen

in the system is $\sim 10^7 M_\odot$, so that it dominates the energetics of the cold phase of the outflow. Taking all these three phases together, the total mass of gas in the outflow approaches $10^8 M_\odot$, and the kinetic energy is at least $6 \times 10^{55} \text{ erg}$ ($v = v_r$), and is $\sim 3.5 \times 10^{56} \text{ erg}$ if $v = v_{\text{shock}}$. The thermal energy in the cold phase is negligible in comparison, but in the hot phase it is substantial, $6 \times 10^{56} \text{ erg}$; however, on the shock model, about half of this energy is not the result of AGN input, but is the internal energy of the unshocked hot gas. Conservatively we take the magnetic field strength in the hot gas to be at the lower limit that we derived from the depolarization calculations, in which case its energy density makes only a small contribution to the total. Finally, the minimum energy stored in the lobes is $\sim 3 \times 10^{56} \text{ erg}$. Putting all this together (Table 4), the AGN must have supplied at least 10^{57} erg over its lifetime. The total estimated work done by the jet in heating and accelerating the various phases of the environment is comparable to (a factor ~ 2 larger than) the *minimum* energy stored in the radio lobes, so that it is plausible that there is rough equality between work done on the environment and lobe energy – this is in agreement with what is seen in numerical simulations of FRIIs that drive shocks into their environments (Hardcastle & Krause, in prep.).

We can use the total energy calculated above to estimate the jet power. The projected length of the NE jet is 2.2 kpc ; thus for uniform expansion⁴ and given the observed radial velocity the lifetime $\tau = d/v = 8 \tan \theta \text{ Myr}$, or 3.5 Myr for $\theta = 24^\circ$ as estimated above, which gives a required time-averaged jet power of $10^{43} \text{ erg s}^{-1}$. Is this a reasonable kinetic luminosity for 3C 305? H10 estimated a jet power around 30 times higher for 3C 171 on a very similar basis, but 3C 171 is a much more powerful source in all other respects⁵ – its low-frequency radio luminosity is about a factor 50 higher, for example – so these numbers seem reasonable from that point of view. A more surprising comparison comes from considering FRI sources. For example, Croston et al. (2009) show that the jet power (including work done on the environment, but considering only one jet) of the closest FRI, Cen A, is $\sim 10^{43} \text{ erg s}^{-1}$. In a very different way, based on their detailed study of the dynamics of the jet combined with X-ray observations of its environment, Laing & Bridle (2002) determine a jet power for the archetypal twin-jet FRI 3C 31, a factor ~ 6 less luminous at low frequencies than 3C 305, of $10^{44} \text{ erg s}^{-1}$. In other words, there appear to be FRI jets whose kinetic powers are comparable to, or even substantially exceed, that of the FRII-like 3C 305 (with its well-collimated, apparently relativistic jets and bright hotspots). Should this come as a surprise? Probably not, since we know that the FRI/FRII transition is both observationally and theoretically a strong function of environment (Ledlow & Owen 1996; Bicknell 1995), and 3C 31 at least inhabits a much richer environment than 3C 305, one in which much of the kinetic power of the jet must be expended in accelerating (and possibly heating) entrained external material. However, the comparison of

⁴ Radio sources probably do not expand uniformly, but for any realistic power-law dependence of lobe length L on time t , the error in assuming $t = L/(dL/dt)$ is of order unity; for example, in the self-similar models of Kaiser & Alexander (1997), $L = Ct^{3/(5-\beta)}$, where β is a power-law exponent of external density defined by Kaiser & Alexander, with $1 < \beta < 3$ from observation: then $L/(dL/dt) = (5 - \beta)t/3$, so the factor by which an assumption of uniform expansion is in error is between $2/3$ and $4/3$.

⁵ Radio luminosity comparisons in this section use the 178-MHz flux densities and low-frequency spectral indices from Laing, Riley & Longair (1983), adjusted to the flux scale of Roger, Bridle & Costain (1973): see <http://3crr.extragalactic.info/>.

Table 4. Contributions to the energetics of the outflow in 3C 305

Phase	Mass (M_{\odot})	Ref.	Internal energy (erg)	Kinetic energy (erg)	Contribution to total (erg)
Hot gas	7×10^7	1	6×10^{56}	3×10^{56}	6×10^{56}
Emission-line gas	4×10^5	2	–	2×10^{54}	2×10^{54}
Cold gas	10^7	2	–	4×10^{55}	4×10^{55}
Magnetic field in hot gas	–	1	$> 10^{55}$	–	10^{55}
Lobes	–	1	$> 3 \times 10^{56}$	–	3×10^{56}
Total					10^{57}

A dash indicates that the quantity in question is negligible. References for gas masses are as follows: (1) This paper; (2) Morganti et al. (2005a). Kinetic energies are calculated on the assumption that $v = 650 \text{ km s}^{-1}$ (see the text). Half the internal energy of the hot phase is assumed to be pre-existing (i.e. it was the internal energy of the unshocked gas) and so does not count towards the total energy input from the radio source.

3C 31 and 3C 305 clearly shows the danger of inferring jet powers directly from radio observations.

One remaining puzzle is why this luminosity is so much less than the line luminosity estimated by H82, $10^{44} \text{ erg s}^{-1}$. H82 themselves noted that there are problems with such a high emission-line luminosity if the optical line-emission regions are ionized by the X-ray-emitting plasma, given that even their upper limit on X-ray emission was $< 10^{42} \text{ erg s}^{-1}$: this problem is made worse by our detection of X-ray emission with a bolometric luminosity of $4.4 \times 10^{41} \text{ erg s}^{-1}$, as we noted in Section 4.2. But our estimates of jet power here, coupled with our belief that all the radiation seen from the system is a result of an interaction between the jet and the external medium, add a further difficulty: it is very hard to see how such a high line luminosity can be powered by a jet that is on average carrying an order of magnitude less power. In fact, it seems very likely that the emission-line luminosity that H82 derive is a significant overestimate. They derive an $E(B - V)$ of 0.85 from the large Balmer decrement they observe, which is confirmed by later observations, e.g. those of Buttiglione et al. (2009); but, as shown by Tadhunter et al. (2005), the stellar continuum in 3C 305 is dominated by an intermediate-age stellar population with strong Balmer line absorption, and, as this is much stronger for $H\beta$ than $H\alpha$, large apparent $H\alpha/H\beta$ ratios are expected without some correction for the underlying continuum, which was not carried out by H82. Although we know from optical imaging observations (e.g. Martel et al. 1999) that there is dust on scales comparable to the emission-line regions, so that some reddening is expected, the $E(B - V)$ values measured for the dusty narrow-line regions of other radio galaxies tend to be $\sim 0.3 - 0.5$ (e.g. Tadhunter et al. 1994; Robinson et al. 2000), and it is unlikely that the value for 3C 305 greatly exceeds these. If we simply assume the Galactic $E(B - V) \approx 0.03$ (from the dust maps of Schlegel et al. 1998) then the line luminosity would come down to $\lesssim 10^{43} \text{ erg s}^{-1}$, and a more realistic correction for the reddening expected from 3C 305 would probably increase this by at most a factor of a few. This luminosity is still high compared to the X-ray emission but is no longer inconsistent with our estimates of jet and AGN power; thus it seems plausible that some combination of shock-ionization from the jet and photoionization from the AGN can give rise to the line emission that we see.

6 SUMMARY AND CONCLUSIONS

We have presented new, sensitive X-ray and radio observations of the nearby, peculiar radio galaxy 3C 305. Our key results are as follows:

- We have argued based on the morphology of the observed

X-rays, and the properties of the X-ray emission attributed to the hidden AGN, that the extended X-ray-emitting plasma is shock-ionized by the jet.

- We have shown that we can construct a self-consistent model in which the X-ray-emitting plasma is, as found previously with 3C 171, plausibly the material responsible for the observed depolarization in the radio, and used this to place a limit, $B > 1.6 \text{ nT}$, on the magnetic field in the external medium.

- Combining the physical conditions estimated from the X-ray and depolarization analysis with what is known about the source dynamics from optical emission-line and neutral-hydrogen studies, we are able to make a complete (if model-dependent) estimate of the energy budget of the radio source. The X-ray-emitting phase dominates the energetics of the (known) phases of external gas, but warm and cold gas also make significant contributions. The work done on the various phases of the environment is comparable to (a factor ~ 2 larger than) the minimum energy stored in the radio lobes.

- From the work done on the environment and the minimum energy calculation we estimate a jet power for the source of $10^{43} \text{ erg s}^{-1}$, accounting for all known phases of the environment with which the jet is interacting.

Our results above demonstrate the value of a complete multi-wavelength view of a radio source in understanding and quantitatively assessing its environmental impact. The (model-dependent) energetic constraints and kinetic luminosities we have derived require both the X-ray observations (since the hot gas dominates the mass budget and has a high energy density) and the optical/HI measurements (since we need velocities to estimate the kinetic energy). Detailed emission-line or HI studies alone, while crucial to tell us about the kinematics, may be failing to see a substantial fraction of the energy supplied by the AGN (e.g. Holt et al. 2011). While there are relatively few low-redshift targets for X-ray investigations of radio-galaxy-driven outflows (Section 1, and below) we hope to apply these techniques to high-redshift objects in the future. A direct test of the crucial assumption in our modelling above – that the X-ray-emitting gas is outflowing at speeds comparable to the other phases – will have to await high-sensitivity observations with calorimeters in the more distant future.

Finally, we return to the question of why 3C 305, and its more powerful counterpart 3C 171, are so atypical for low-redshift objects in their radio morphology and their relationship with the extended emission-line and X-ray gas. In H10 we argued that the key feature that distinguishes these objects from more typical radio galaxies of the same jet/radio power is a strong interaction between the jet and *cold* gas aligned along the radio axis, since we know that considerably larger amounts of hot gas, even if asymmetrically

distributed, do not prevent the formation of a typical FR II radio galaxy. This picture seems to be consistent with everything we see in 3C 305. The smoking gun for this model in 3C 305 is the presence of neutral hydrogen in outflow along the jet axis (Morganti et al. 2005a). This is very hard to understand in isolation – how can the jet drive neutral hydrogen without disrupting it? – but easier once we realise that the HI is only a small fraction of the outflowing gas. In this picture, then, the jet in 3C 305 has driven a shock into a medium which had originally had a much larger mass of HI and other cold/warm material, aligned along the jet axis and embedded in the hot-gas environment expected for a massive elliptical galaxy. The shock has heated much of the cold gas to high temperatures and shredded the rest, and the remaining HI and other warm-phase material (e.g. the optical emission-line clouds) are being carried along within the outflowing X-ray emission. As noted above, this may help to explain the low abundance derived from APEC fitting to the hot gas. The X-ray ‘wings’, in this picture, must then be shocked material which has been driven back towards the centre of the galaxy by the expanding radio lobes. A somewhat similar scenario (with a similar impact on radio morphology) is seen in the simulations of Wagner & Bicknell (2011). As we remarked in H10, it seems likely that the rarity of similar objects at low redshift (in contrast to the much more typical ‘classical double’ morphology) reflects the rarity of gas-rich mergers in the massive elliptical hosts of local radio galaxies, but this type of interaction is almost certainly both more common and energetically more significant in the earlier universe.

ACKNOWLEDGEMENTS

We thank the referee, Clive Tadhunter, for constructive comments that have helped us to improve the paper. MJH thanks the Royal Society for a Research Fellowship which supported the early parts of this work. The work at SAO was supported by NASA grant G01-12133A. FM acknowledges the Fondazione Angelo Della Riccia for the grant awarded to support his research at SAO during 2011 and the Foundation BLANCEFLOR Boncompagni-Ludovisi, née Bildt, for the grant awarded to him in 2010. The National Radio Astronomy Observatory is a facility of the National Science Foundation operated under cooperative agreement by Associated Universities, Inc.

APPENDIX A: ERROR ESTIMATES FOR HARDNESS RATIOS

In the limit of large numbers of counts, error estimates for hardness ratios can be derived using standard propagation of error techniques. However, we are using hardness ratios precisely because we are too photon-limited to do anything else (e.g. detailed spectral analysis), particularly in the hard band, and so we have to consider uncertainties more carefully. Our analysis differs from that of Gehrels (1986) in being explicitly Bayesian; we focus not on the ‘errors’ on the measured values but on the uncertainties on the inferred quantities of interest. Park et al. (2006) have investigated the Bayesian approach to this problem in some detail, but the generality of their approach leads to a quite complicated solution. Here we describe a simple analysis which is valid in the limit in which the

background can be neglected, and which gives identical results to those of Park et al. in this limit⁶.

Poisson statistics are described by the familiar equation

$$p(n|\mu) = \frac{\mu^n e^{-\mu}}{n!} \quad (\text{A1})$$

where μ is a known expected number of counts and n , an integer, is the number of counts actually observed. We are in the position, though, of observing a given number of counts n and wanting to infer the underlying expected number μ . In this case, by Bayes’ theorem (and assuming an uninformative, though improper, prior) we know that

$$p(\mu|n) = \mu^n e^{-\mu} / \int_0^\infty \mu^n e^{-\mu} d\mu \quad (\text{A2})$$

The normalizing integral here is just the gamma function, $\Gamma(n+1)$, so we can write down the posterior probability distribution of the expected number of counts μ :

$$p(\mu|n) = \frac{\mu^n e^{-\mu}}{\Gamma(n+1)} \quad (\text{A3})$$

This probability distribution is known as the gamma distribution. The maximum-likelihood value of μ (the posterior mode) is, as expected, n . The mean of the distribution is $n+1$ and variance $n+1$, and it converges to a Gaussian in the limit of large n , so we then recover the standard result that the best estimate of μ is $\mu \approx n \pm \sqrt{n}$. In general, though, we would want to estimate the errors on μ by defining a ‘credible interval’ analogous to those used in the case of a Gaussian: for example, the 1σ error range $\mu_l - \mu_h$ could be defined by

$$\int_{\mu_l}^{\mu_h} p(\mu|n) d\mu = \text{erf}(1/\sqrt{2}) = 0.6823 \quad (\text{A4})$$

subject to the constraint that $\mu_h - \mu_l$ takes its minimal value.

Now consider a hardness ratio H , defined as in the text. In an experiment in which two sets of numbers of counts μ_1 and μ_2 could be measured with arbitrary precision, we would expect

$$H = 1 + \frac{\mu_2 - \mu_1}{\mu_2 + \mu_1} \quad (\text{A5})$$

However, in fact, our measurements of numbers of counts n_1 and n_2 give us probability distributions for μ_1 and μ_2 according to eq. A3 above. Consequently there is a probability distribution for H , $p(H|n_1, n_2)$. Our best estimate of H would, again, be $\int H p(H|n_1, n_2) dH$ and the error estimates should be derived in a way analogous to that given in eq. A4.

We cannot easily write down the probability distribution for H analytically, but it is easy to determine it by Monte Carlo simulation. We know $p(\mu_1|n_1)$ and $p(\mu_2|n_2)$ from eq. A3 and so, drawing values of μ_1 and μ_2 from this distribution (we use the GNU Scientific Library function `gsl_ran_gamma`), we can calculate H for each pair from eq. A5. This gives us a set of H values drawn from $p(H)$, from which we can trivially calculate the Bayesian estimator of H (the posterior mean) and the 1σ credible interval. Credible interval calculations for a confidence limit CL will be accurate so long as $N(1-CL) \gg 1$: we use $CL = 0.6823$ and $N = 50000$ in the results presented in the text.

We should note that the use of the posterior mean can give some slightly non-intuitive results in the limit of small n_1, n_2 . For

⁶ We tested this with the code made available at <http://hea-www.harvard.edu/AstroStat/BEHR/>.

example, consider the case where $n_2 = 0$, $n_1 > 0$. Simply calculating the H values from the counts, we expect $H = 0$. But for $n_2 = 0$, the posterior probability distribution of μ_2 , eq. A3, reduces to the exponential distribution, whose mean is not zero: in other words, given our assumptions, the Bayesian estimator of $\mu_2 > 0$ even though we measure no counts and though the maximum-likelihood estimator of $\mu_2 = 0$. Consequently we expect the Bayesian estimator of H , and its 1σ confidence limits, to be > 0 . As it is computationally simpler to calculate the Bayesian estimator and its credible interval from the Monte Carlo than it is to do the same for the maximum-likelihood estimate, we plot the Bayesian estimator of H in Fig. 9 in the text.

REFERENCES

- Baum, S.A., Heckman, T., 1989, *ApJ*, 336, 681
 Bianchi, S., Guainazzi, M., Chiaberge, M., 2006, *A&A*, 448, 499
 Bicknell, G.V., 1995, *ApJS*, 101, 29
 Böhringer, H., Nulsen, P.E.J., Braun, R., Fabian, A.C., 1995, *MNRAS*, 274, L67
 Buote, D.A., Fabian, A.C., 1998, *MNRAS*, 296, 977
 Buttiglione, S., Capetti, A., Celotti, A., Axon, D.J., Chiaberge, Macchetto, F.D., Sparks, W.B., 2009, *A&A*, 495, 1033
 Carilli, C.L., Harris, D.E., Pentericci, L., Röttgering, H.J.A., Miley, G.K., Kurk, J.D., van Breugel W., 2002, *ApJ*, 567, 781
 Clark, N.E., Axon, D.J., Tadhunter, C.N., Robinson, A., O'Brien, P., 1998, *ApJ*, 494, 546
 Croston, J.H., Hardcastle, M.J., Birkinshaw, M., Worrall, D.M., 2003, *MNRAS*, 346, 1041
 Croston, J.H., et al. 2009, *MNRAS*, 396, 1999
 Dicken, D., Tadhunter, C., Axon, D., Robinson, A., Morganti, R., Kharb, P., 2010, *ApJ*, 722, 1333
 Evans, D.A., Hardcastle, M.J., Lee, J.C., Kraft, R.P., Worrall, D.M., Birkinshaw, M., Croston, J.H., 2008, *ApJ*, 688, 844
 Garrington, S., Leahy, J.P., Conway, R.G., Laing, R.A., 1988, *Nat*, 331, 147
 Gehrels, N., 1986, *ApJ*, 303, 336
 Hardcastle, M.J., 2003, *MNRAS*, 339, 360
 Hardcastle, M.J., Alexander, P., Pooley, G.G., Riley, J.M., 1997, *MNRAS*, 288, 859
 Hardcastle, M.J., Evans, D.A., Croston, J.H., 2009, *MNRAS*, 396, 1929
 Hardcastle, M.J., Massaro, F., Harris, D.E., 2010, *MNRAS*, 401, 2697
 Hardcastle, M.J., Kraft, R.P., Worrall, D.M., Croston, J.H., Evans, D.A., Birkinshaw, M., Murray, S.S., 2007, *ApJ*, 662, 166
 Hardcastle, M.J., Sakelliou, I., Worrall, D.M., 2005, *MNRAS*, 359, 1007
 Heckman, T.M., Miley, G.K., Balick, B., van Breugel, W.J.M., Butcher, H.R., 1982, *ApJ*, 262, 529 [H82]
 Heckman, T.M., van Breugel W.J.M., Miley, G.K., 1984, *ApJ*, 286, 509
 Heckman, T.M., Illingworth, G.D., Miley, G.K., van Breugel W.J.M., 1985, *ApJ*, 299, 41
 Heckman, T.M., Ptak, A., Hornschemeier, A., Kauffmann, G., 2005, *ApJ*, 634, 161
 Holt, J., Tadhunter, C., Morganti, R., Bellamy, M., González, Delgado, R.M., Tzioumis, A., Inskip, K.J., 2006, *MNRAS*, 370, 1633
 Holt, J., Tadhunter, C.N., Morganti, R., Emonts, B.H.C., 2011, *MNRAS*, 410, 1527
 Jackson, N., Beswick, R., Pedlar, A., Cole, G.H., Sparks, W.B., Leahy, J.P., Axon, D.J., Holloway, A.J., 2003, *MNRAS*, 338, 643
 Johnson, R., Finoguenov, A., Ponman, T.J., Rasmussen, J., Sanderson, A.J.R., 2011, *MNRAS*, 413, 2467
 Kaiser, C.R., Alexander, P., 1997, *MNRAS*, 286, 215
 Laing, R.A., 1988, *Nat*, 331, 149
 Laing, R.A., Bridle, A.H., 2002, *MNRAS*, 336, 1161
 Laing, R.A., Riley, J.M., Longair, M.S., 1983, *MNRAS*, 204, 151
 Ledlow, M.J., Owen, F.N., 1996, *AJ*, 112, 9
 Liszt, H., 2001, *A&A*, 371, 398
 Martel, A.R., et al., 1999, *ApJS*, 122, 81
 Massaro, F., et al., 2009, *ApJ*, 692, L123 [M09]
 Massaro, F., et al., 2010, *ApJ*, 714, 589
 McCarthy, P.J., 1993, *ARA&A*, 31, 639
 McCarthy, P.J., Baum, S., Spinrad, H., 1996, *ApJS*, 106, 281
 McCarthy, P.J., van Breugel, W., Spinrad, H., Djorgovski, S., 1987, *ApJ*, 321, L29
 Miller, N.A., Ledlow, M.J., Owen, F.N., Hill, J.M., 2002, *AJ*, 123, 3018
 Morganti, R., Oosterloo, T.A., Tadhunter, C.N., van Moorsel, G., Emonts, B., 2005a, *A&A*, 439, 521
 Morganti, R., Tadhunter, C., Oosterloo, T.A., 2005b, *A&A*, 441, L9
 Nesvadba, N.P.H., Lehnert, M.D., De Breuck, C., Gilbert, A.M., van Breugel W., 2008, *A&A*, 491, 407
 O'Dea, C.P., Baum, S.A., Gallimore, J.F., 1994, *ApJ*, 436, 669
 O'Dea, C.P., et al., 2002, *AJ*, 123, 2333
 Osmond, J.P.F., Ponman, T.J., 2004, *MNRAS*, 350, 1511
 Park, T., Kashyap, V.L., Siemiginowska, A., van Dyk D.A., Zezas, A., Heinke, C., Wargelin, B.J., 2006, *ApJ*, 652, 610
 Privon, G.C., O'Dea, C.P., Baum, S.A., Axon, D.J., Kharb, P., Buchanan, C.L., Sparks, W., Chiaberge, M., 2008, *ApJS*, 175, 423
 Robinson, T.G., Tadhunter, C.N., Axon, D.J., Robinson, A., 2000, *MNRAS*, 317, 922
 Schlegel, D.J., Finkbeiner, D.P., Davis, M., 1998, *ApJ*, 500, 525
 Sólórzano-Iñárrrea, C., Tadhunter, C.N., Bland-Hawthorn, J., 2002, *MNRAS*, 331, 673
 Tadhunter, C., 2007, *NewAR* 51 153
 Tadhunter, C.N., Metz, S., Robinson, A., 1994, *MNRAS*, 268, 989
 Tadhunter, C.N., Morganti, R., Robinson, A., Dickson, R., Villar-Martin, M., Fosbury, R.A.E., 1998, *MNRAS*, 298, 1035
 Tadhunter, C., Robinson, T.G., González, Delgado, R.M., Wills, K., Morganti, R., 2005, *MNRAS*, 356, 480
 Wagner, A.Y., Bicknell, G.V., 2011, *ApJ*, 728, 29
 Weaver, K.A., Mushotzky, R.F., Serlemitsos, P.J., Wilson, A.S., Elvis, M., Briel, U., 1995, *ApJ*, 442, 597